Contract No. and Disclaimer:

Ag Nanoparticle Embedded TiO_2 Composite Nanorod Arrays Fabricated by Oblique Angle Deposition: Toward Plasmonic Photocatalysis

Simona E. Hunyadi Murph,[a]

Yizhuo He,[b] Pradip Basnet,[b] and Yiping Zhao[b]

[a] *Savannah River National Laboratory, Aiken, SC, 29808, USA*

[b] *Department of Physics and Astronomy, and Nanoscale Science and Engineering Center, University of Georgia, Athens, Georgia 30602*

Abstract

Using a unique oblique angle co-deposition technique, well aligned arrays of Ag nanoparticle embedded TiO_2 composite nanorods have been fabricated with different concentrations of Ag. The structural, optical and photocatalytic properties of the composite nanostructures are investigated using a variety of experimental techniques and compared with those of pure TiO_2 nanorods fabricated similarly. Ag nanoparticles are formed in the composite nanorods, which increase the visible light absorbance due to localized surface plasmon resonance. The Ag concentrations and the annealing conditions are found to affect the size and the density of Ag nanoparticles and their optical properties. The Ag nanoparticle embedded TiO_2 nanostructures exhibit enhanced photocatalytic activity compared to pure TiO_2 under visible- or UV-light illumination. Ag plays different roles in assisting the photocatalysis with different light sources. Ag can be excited and inject electrons to TiO_2, working as an electron donor under visible light. While under UV illumination, Ag acts as electron acceptor to trap the photogenerated electrons in TiO_2. Due to the opposite electron transfer direction under UV and visible light, the presence of Ag may not result in a greater enhancement in the photocatalytic performance.

Keywords: Oblique angle co-deposition; Nanorods; Plasmonic photocatalyst; Ag nanoparticle embedded TiO_2

1. Introduction

Nanostructured titanium dioxide (TiO_2) has attracted great attention among various semiconductor photocatalysts due to its promising performance in many applications, such as water splitting,[1-3] and CO_2 photoreduction.[4-7] However, it is well known that the large band gap (~ 3.2 eV) and the fast electron-hole recombination limit the photoresponse spectral range and the practical efficiency of intrinsic TiO_2 as a photocatalyst. Several strategies such as doping with non-metal (NO_x and N),[8, 9] doping with metal (Cr and V),[10-12] dye sensitization,[13] and coupled with other semiconductors,[14] have been proposed to circumvent these problems. The addition of noble metal to TiO_2, such as Pt,[15] has been demonstrated as an effective way to improve the photocatalytic efficiency because noble metal can trap the photogenerated electrons in TiO_2 and inhibit the charge recombination process.[16, 17]

Recently, plasmonic photocatalysis has been proposed to extend the photocatalytic activity of TiO_2 to visible light range. Generally, plasmonic photocatalysts are mixtures of semiconductors and noble metal nanoparticles (NPs). The semiconductors usually absorb UV or visible light and then generate electron-hole pairs that will participate in photocatalytic reaction. The noble metal NPs usually have strong absorption in visible region due to localized surface plasmon resonance (LSPR). From the energy conversion point of view, if the energy of the absorbed visible light by noble metal NPs can be utilized to improve photocatalytic reaction rates, then the coupled semiconductor-metal system is a plasmonic photocatalyst. There are three possible mechanisms for plasmonic photocatalysts to extend the photocatalytic performance to visible light range. First, the noble metal nanoparticles can be directly coupled

to semiconductors so that the photogenerated electrons or holes due to LSPR absorbance in metal NPs may be transferred to semiconductors, resulting in enhanced photocatalytic performance.[18] But direct contact of semiconductor with noble metal can also lead to back transfer of charges from semiconductors to noble metal NPs. Another possible mechanism is that when semiconductors and noble metals are spatially separated, the excited noble-metal NPs can transfer the absorbed energy to semiconductors in a radiative way through localized interaction of semiconductors with the LSPR-induced enhanced localized electric field.[19] In addition, the heat generated through LSPR absorbance by metal NPs could be a third possible mechanism in some cases. The high absorbance of metal NPs at LSPR wavelength can heat the surroundings locally due to the nonradiative decay of surface plasmons to phonons, and therefore accelerate the photocatalytic reactions by increasing the local temperature around semiconductors.[20]

Among the proposed plasmonic photocatalysts, Ag-TiO_2 composites have been widely studied and prepared by a variety of methods. In many studies, Ag NPs are loaded on the surface of TiO_2 by different techniques, such as, radio-frequency (RF) sputtering,[21] photo-deposition,[22] and electrostatic force directed assembly (ESFDA) method.[23] Enhancement in photocatalytic activity has been observed with these Ag-TiO_2 samples. However, since most Ag is on the surface of TiO_2, the surface area of TiO_2 exposed to illumination is reduced and also the interface between Ag and TiO_2 is limited. In order to facilitate the charge transfer process, the interface between Ag and TiO_2 should be maximized. A better design could be achieved by simply mixing Ag NPs toTiO_2 structures. This has been

realized by sol-gel method.[24, 25] However, sol-gel method usually needs precursors and may have organic residues in the samples. Moreover, a good control over the structure of samples is hard to achieve via sol-gel method. A better strategy is to make Ag-TiO_2 porous nanostructures directly through physical means.

Oblique angle co-deposition, which combines co-deposition and oblique angle deposition (OAD), has been repeatedly demonstrated as a powerful technique to fabricate well-aligned composite nanostructures.[26-31] OAD is a well-known physical vapor deposition technique in which the vapor flux is incident onto a substrate at a large incident angle (> 70^o) with respect to the substrate normal. Generally, well-aligned and tilted nanorod arrays are formed due to geometric shadowing effect. The morphological parameters of the nanorod array such as the tiling angle, nanorod length, nanorod density, etc., can be tuned by varying the deposition conditions such as deposition angle, rate, time, and temperature. In co-deposition, two or more materials are evaporated simultaneously and then deposited on the substrates to produce composite materials, of which the composition can be easily controlled by varying the relative ratio of the deposition rates of the two materials. Therefore, by combining OAD and co-deposition, composite nanorod arrays with tunable morphology and composition can be fabricated. Recently we have successfully fabricated Ag NP embedded MgF_2,[27] Cr doped TiO_2,[28] CdSe-TiO_2,[29] Si-Cu,[31] and Si-Cu composition graded nanorods,[32] by oblique angle co-deposition (OACD) method. Typically, Ag NPs are embedded in MgF_2 and exhibit LSPR properties, which suggests that it is possible to fabricate TiO_2 nanorods with Ag NPs embedded as a plasmonic photocatalyst using OACD method.

In this work, Ag NP embedded TiO_2 composite nanorod arrays of various Ag concentrations are prepared by OACD. The structural, optical and photocatalytic properties are characterized and compared with those of pure TiO_2, which is fabricated by a single-source OAD technique. Ag nano-clusters are found to segregate out of the TiO_2 matrix and form nanoparticles. The size and the density of Ag NPs are greatly affected by the concentrations of Ag and post-deposition annealing condition. These Ag NPs extend the absorbance of the composite nanorods into visible region. Furthermore, the photocatalytic activity is tested by Methylene Blue (MB) degradation under visible- and UV-light illumination. Ag NP embedded TiO_2 is found to exhibit better catalytic performance compared to intrinsic TiO_2 and the functionality of Ag NPs is different under different illumination.

2. Experimental

TiO_2 and Ag NP embedded TiO_2 nanorod arrays were fabricated using OACD technique in a custom designed vacuum deposition system (Pascal Technology) equipped with two electron-beam evaporation sources. The details of the deposition system can be found elsewhere.[33] Pre-cleaned glass microscopic slides (Gold seal® Catalog No. 3010) and Si (100) wafers were used as substrates. Before deposition, the chamber was evacuated to the pressure of 8×10^{-7} Torr. The TiO_2 (99.9%, Kurt J. Lesker) and Ag (99.999%, Kurt J. Lesker) sources were evaporated under a pressure around 5×10^{-6} Torr. The deposition vapor flux was incident onto substrates at an angle of 87° with respect to the substrate normal. Two separate quartz crystal microbalances (QCMs) were used to independently monitor the deposition rates r_{Ag}

and r_{TiO_2} respectively during the deposition. By changing the relative ratio of r_{Ag} and r_{TiO_2}, the atomic ratio of Ag in the composite X% could be tuned following the relation,

$$X/(100-X) = (\rho_{Ag} r_{Ag} / M_{Ag}) : (\rho_{TiO_2} r_{TiO_2} / M_{TiO_2}), \quad (1)$$

where ρ and M are the density and molar mass of the corresponding material, respectively. All these samples were denoted as X%Ag-TiO_2 and X% is the atomic ratio of Ag in the composite, defined as $X\% = N_{Ag}/(N_{Ag}+N_{Ti})$, where N_{Ag} and N_{Ti} represent the number of Ag and Ti atoms in the composite. In this study X% was designed to be 0%, 5%, 10%, 15% and 20%, respectively. The corresponding deposition rates of Ag and TiO_2 are listed in Table 1. A total QCM thickness reading of 2 μm was reached at the end of each deposition, i.e.

$$d_{Ag}^{QCM} + d_{TiO_2}^{QCM} = 2\mu m. \quad (2)$$

After the deposition, the nanorod samples were annealed in an argon atmosphere in a quartz tube furnace (Lindberg/Blue M Company) with an argon flow rate of 230 SCCM. During the annealing, the samples were heated to 400^{o}C and 500^{o}C respectively at a heating rate of 5^{o}C/min and subsequently annealed for 4 hrs. Then the samples were cooled down to room temperature in argon atmosphere. These processes could prevent the oxidation of Ag in the composite.

The morphologies and compositions of the nanorod arrays were characterized by a field-emission scanning electron microscope (SEM) equipped with an energy dispersive X-ray spectroscopy (EDX) (FEI Inspect F). Each sample was analyzed by X-ray diffraction (XRD) (PANanalytical X'Pert PRO) to confirm the crystal structures, using Cu *Kα* radiation with the

X-ray incident angle of 0.5°. The optical properties were characterized by an UV-Vis-NIR double beam spectrophotometer (JASCO V-570) equipped with two rotatable Glan Thompson polarizers (Thorlabs Inc.). The photocatalytic activities of both Ag NP embedded TiO_2 and pure TiO_2 nanorod arrays were evaluated by the photocatalytic degradation of a 10 ppm Methylene Blue (MB; $C_{16}H_{18}ClN_3S$, Alfa Aesar, CAS #122965-43-9) aqueous solution, under ultraviolet (UV; BLAK-RAY, Model B 100AP), visible (250 W quartz halogen lamp: UtiliTech) and UV plus visible light irradiation. Typically, the prepared MB aqueous solution had a pH value of 6.2 at room temperature. The samples on glass substrates (8 mm × 25.4 mm) were placed into a 10 mm × 10 mm × 45 mm clear methacrylate cuvette, filled with 4.0 ml of 10 ppm MB aqueous solution. Prior to the irradiation, each sample was kept in dark for 30 min, to ensure equilibrium of the dye adsorption on the surface of the photocatalysts. Then the samples were exposed to different illumination conditions for 4 hrs. The UV light at wavelength of 365 nm had a power density about 10 mW/cm^2 at the position of the cuvette as measured by a UV power meter (Fisher Scientific, UVA-365) and the visible light with wavelength range of 400 nm to 800 nm had a power density about 65 mW/cm^2 at the position of the cuvette, as measured by a thermal optical power meter (Thorlabs PM100D/S310C); and the position of light sources were adjusted in such a way that the sample was facing towards UV light and opposite to the visible light source. A water filter was placed near the cuvette on the visible light source side to absorb the IR radiation. Then the degradation of MB aqueous solution was quantified by recording the optical absorption spectra of the remaining MB solution every 30 minutes in situ using a USB 2000 Ocean Optics spectrophotometer. The time

evolution of absorbance peak at λ = 664 nm was used to evaluate the photodecay rate.

3. Results

3.1. Composition of Ag-TiO_2 nanocomposites

The qualitative composition of the Ag NP embedded TiO_2 samples were determined by EDX measurements. The EDX spectra of as-deposited samples are shown in Fig. S1 in Supporting Information. The results along with the deposition conditions are summarized in Table 1. As shown in Table 1, the EDX measurements confirm that the measured Ag atomic ratio *X'* % have the same trend with the designed *X* %, but *X'* % is always larger than *X* %. In this paper, the designed Ag atomic ratio in the composite *X* % will be used throughout the context to refer to the nanorod samples.

3.2. Morphology of Ag-TiO_2 composite nanorod arrays

The representative top view and cross-sectional view SEM images of as-deposited and annealed Ag-TiO_2 composite samples are shown in Fig. 1. For as-deposited films, as indicated by the SEM images (first two rows in Fig. 1), tilted nanorod arrays are formed on the substrates with different doping concentrations of Ag. The nanorod density is estimated to be approximately 9 ± 1 rods/μm^2 for each sample. The nanorods fan out along the direction perpendicular to the incident vapor flux due to the lack of shadowing effect in this direction.[34] The width at the top of nanorods along the fan-out direction is approximately 300 ± 100 nm, while the width perpendicular to the fan-out direction is approximately 50 ± 10 nm for all the as-deposited samples. From the cross-sectional view SEM images, the tilting angles β, defined

as the angle of nanorod with respect to the surface normal of substrate, and the vertical heights *h* of the as-deposited nanorods are measured and summarized in Table 1, and are plotted versus *X'* % in Fig. 2. The tilting angle β is about 55° for the intrinsic TiO_2 nanorods and gradually increases with *X'* %, and finally reaches 71° for pure Ag nanorods.[35] Based on a semi-empirical statistic model that describes the tilting angle of composite nanorods,[36] by assuming that the effective radii of Ag atom and TiO_2 molecule are 145 pm and 200 pm respectively, the β of the composite nanorods can be expressed as,

$$\beta = 39.33(X'\%)^3 - 66.06(X'\%)^2 + 42.65X'\% + 54.96 . \quad (3)$$

As shown in Fig. 2, the fitting by the statistic model agrees well with the experimental data. The increase of Ag concentration in TiO_2 nanorods also leads to smaller vertical nanorod heights as plotted in Fig. 2. The heights of the nanorods *h* can be fitted by a model assuming that the contribution of each material is proportional to the QCM thickness d^{QCM},

$$h = h_{Ag} + h_{TiO_2} = A_{Ag} d_{Ag}^{QCM} + B_{TiO_2} d_{TiO_2}^{QCM} , \quad (4)$$

where A_{Ag} and B_{TiO_2} are coefficients related to deposition conditions. Combined with Eqs. (1) and (2), the final expression for *h* in terms of *X'* % is,

$$h = A_{Ag} \frac{1.08X'}{100 - 0.46X'} + B_{TiO_2}(2 - \frac{1.08X'}{100 - 0.46X'}) . \quad (5)$$

However, the best fitting gives A_{Ag} = -0.4 ± 0.2 and B_{TiO_2} = 0.68 ± 0.03. An explanation for the negative A_{Ag} value is that Ag atoms are incorporated into TiO_2 voids and reduce the porosity of the composite nanorods as we can see in later discussion for TEM results. After the composite nanorods annealed in argon, there is no distinct change in β and *h*.

From these SEM images, Ag NPs are observable on the surface of the nanorods. The average sizes or diameters D_{NP}, and densities n_{NP}, defined as the particle numbers per unit surface area of nanorods, of these nanoparticles under different thermal treatments are summarized in Table 2 and the particle size distributions are plotted in bottom row of Fig. 1. In the as-deposited samples, only a few nanoparticles can be observed. After annealing in argon at $T = 400^{o}$C, the nanoparticle densities increase dramatically, especially in small size range (< 70 nm) and decrease significantly after annealing at $T = 500^{o}$C. In addition, larger Ag NPs can be observed after annealing at $T = 500^{o}$C. From the statistics on Ag NPs, we find the following general trend: for the samples under the same thermal treatment condition, the average particle size increases with X %, in the meantime, the variation of particle size becomes larger. These Ag NPs are formed through the diffusion and the coalescence of silver atoms or clusters. The diffusion and coalescence of metal nanoparticles has already been studied,[37] which indicates that the high surface energy of small metal particles leads to the coalescence of particles in order to minimize the total surface energy. The energy for the diffusion and coalescence of metal particles mainly comes from the thermal background. During the deposition, the substrate temperature was risen to less than 100^{o}C. Moreover, the silver can be easily oxidized during the co-deposition where oxygen species are present. It is known that oxidation occurs on the surface of Ag NPs even at room temperature when exposed to oxygen.[38] Therefore, during the deposition, the diffusion and coalescence of Ag clusters or nanoparticles may be limited by both the low substrate temperature and potentially the formation of silver oxide film on Ag NPs or clusters. As a result, most of Ag atoms or clusters are hidden within the TiO_2 matrix and

cannot diffuse out to the surface to form large nanoparticles in as-deposited samples could be too small to be seen in SEM. This may explain why only a few nanoparticles can be observed on the as-deposited samples.

The annealed nanorods have more and larger nanoparticles than as-deposited nanorods because the high temperature during annealing process provides sufficient energy for the diffusion and coalescence of Ag NPs. High temperature also enables the thermal decomposition of silver oxide into metallic silver and oxygen,[39] which is in favor of diffusion and coalescence. In addition, Ag atoms cannot enter the TiO_2 lattice to form a stable solid solution because the Ag^+ ion (126 pm) has a much larger radius than that of Ti^{4+} ion (68 pm).[40] We propose that the annealing process segregates the Ag atoms from TiO_2 matrix, allows the migration to the surface of TiO_2 nanorods, and results in aggregation into larger clusters or particles by coalescence, forming new nanoparticles on the surface. This can explain the density increase of Ag NPs after annealing at $T = 400^oC$. The annealing process with a higher temperature at $T = 500^oC$ provides more thermal energy compared with the annealing at $T = 400^oC$, which leads to further diffusion and coalescence of Ag NPs. At $T = 500^oC$, the coalescence of Ag NPs on the surface is the prevailing process instead of the migration of Ag clusters to the surface. The further coalescence of Ag NPs decreases the Ag NP densities and in the meantime increases the Ag NP sizes.

The particle distribution of Ag-TiO_2 composite is also confirmed by TEM measurement. The representative TEM images of as-deposited and annealed 20%Ag-TiO_2 (500^oC) samples are shown in Fig. 3. The Ag NPs can be clearly observed from the TEM images. Before

annealing, each nanorod backbone exhibits fibrous structures, which is consistent with previous study.[41] But after annealing at 500°C in argon, no fibrous structures are observable. Instead, many vacancies appear on the nanorods as shown in Fig 3 (b). As proposed above, during the annealing process, Ag clusters and nanoparticles may diffuse and coalesce with each other, which may leave vacancies in the TiO_2 matrix. It is also possible that some vacancies may already exist in the as-deposited TiO_2. During the crystallization of TiO_2, the vacancies can diffuse and coalesce with each other and form the large and noticeable vacancies as shown in TEM images.

3.3. XRD characterization

The XRD spectra of both pure TiO_2 and Ag NP embedded TiO_2 nanorods were taken to confirm the crystal structures of the composites as shown in Fig. 4. For the as-deposited samples, Figure 4 (a) shows no diffraction peaks associated with crystalline TiO_2, demonstrating that TiO_2 in both the as-deposited intrinsic and composite samples are amorphous. There are very weak diffraction peaks associated with Ag observed at $2\theta = 38.1°$, 44.3°, 64.5°, and 77.4° in Ag NP embedded TiO_2 samples, corresponding respectively to the (111), (200), (220), and (311) crystal planes of Ag. The peaks become more intense as X % increases. No diffraction peaks of silver oxide are observed, indicating either that there is a very small amount of silver oxide in as-deposited samples, which is beyond the detection limit of the instrument, or the silver oxides are in amorphous state.

After annealing at 400°C and 500°C in argon, the diffraction peaks corresponding to TiO_2

anatase phase are observed at 2θ = 25.3°, 37.8°, 48.1°, 53.9°, 55.1°, 62.7°, 68.8°, 70.2°, and 77.4°, corresponding respectively to the (101), (004), (200), (105), (211), (204), (116), (220), and (215) crystal planes of TiO_2 anatase phase, as shown in Figs. 4 (b) and (c). The diffraction peak positions of Ag almost remain the same, while the diffraction intensities become more significant demonstrating more Ag are forming crystal clusters compared to as-deposited samples. This observation is consistent with SEM and TEM observations, and indicates that part of Ag and TiO_2 are incorporated in amorphous state while part of Ag aggregates into small crystals for the as-deposited samples.

By applying Scherrer's formula, the average grain sizes of TiO_2 were estimated using the strongest peaks (101) for anatase and are summarized in Table 2. Higher annealing temperature leads to larger grain sizes except for the 20%Ag-TiO_2 samples. It has been widely accepted that the presence of silver in TiO_2 matrix has an inhibition effect on the growth of anatase phase.[40, 42, 43] However, in our case, the TiO_2 grain sizes first increase and then decrease as X % increases.

3.4. Optical properties

The optical properties of TiO_2 and Ag-TiO_2 nanorod arrays were characterized by UV-Vis spectroscopy. Figure 5 shows the extinction spectra, extracted from transmission spectra of both intrinsic TiO_2 and Ag-TiO_2 nanorod films with unpolarized incident light. For all the as-deposited or annealed samples, strong extinction in UV region is primarily attributed to the absorption of TiO_2. Moreover, Ag loading and annealing conditions also affect the extinction

spectra.

For all the as-deposited composite samples, no distinct feature of LSPR of Ag NPs is observed possibly due to low density of Ag NPs. The extinction in the visible region increases with increasing Ag concentration, though the film thickness decreases monotonically. It keeps almost the same trend in UV region except for the 10%Ag-TiO_2 sample. This increase of extinction over the broad spectrum is mainly attributed to the absorption and scattering of Ag atoms and nanoparticles in as-deposited films.

After annealed in argon, the extinction spectra of TiO_2, 5% and 10%Ag-TiO_2 composite samples almost overlap with each other in visible region. However, a very broad extinction peak is observed in the wavelength range of 500 ~ 700 nm in the spectra of 15% and 20% Ag-TiO_2 samples due to LSPR of metallic Ag NPs. The position of the LSPR peak of Ag NPs is determined by both their size and the refractive index of the host matrix. A broad LSPR peak results from a wide distribution of Ag nanoparticle sizes. In addition, the samples annealed at 400^{o}C have more intense extinction peak around 600 nm than those annealed at 500^{o}C. This is mainly due to the fact that the density of Ag NPs annealed at 400^{o}C is much higher than that annealed at 500^{o}C as shown in Fig. 1.

The optical properties of TiO_2 and Ag-TiO_2 nanorod films can be estimated using an effective medium theory (EMT).[44] The EMT of oblique columnar structures has already been well developed.[45, 46] Maxwell-Garnett (MG) approximation is first used to estimate the effective refractive index of the bulk TiO_2 with Ag NP composite, and then a Bruggeman (Br) approximation is applied to estimate the effective refractive index of the Ag-TiO_2 nanorod

arrays, i.e. the void-Ag-TiO_2 composite structures. The nanorods can be treated as prolate spheroids. The detailed calculations are presented in the Supporting Information (Part II) and the calculated absorption spectra are plotted in Fig. 6 in comparison with the experimental spectra of the composite nanorod films annealed at 500^{o}C, measured by the polarized UV-Vis. As demonstrated by the calculations, a distinct absorption peak centered at about 550 nm appears in the spectra of all Ag-TiO_2 composite nanorod films and it becomes more intense as the concentration of silver increases. This is consistent qualitatively with the experimental data. It should be noted that scattering or reflection is not taken into accounts in the calculations, which actually happens in the UV-Vis measurements and affects the determination of extinction spectra. In addition, the wavelength of LSPR peak varies with the size of Ag NPs, which will broaden the actual absorbance peak. This may explain why the experimental extinction peak is much less intense than the calculated one even at high X %. In addition, the calculation based on EMT indicates that the nanorod films absorb more p-polarized light than s-polarized across the whole UV-Vis region. This also agrees well with the experimental data at short wavelength region, while the extinction at long wavelengths does not vary much between s- and p-polarized incident lights.

3.5. Photocatalytic activity

In order to study the effect of Ag loading in TiO_2 on the photocatalytic activities, MB photodegradation experiments were performed under UV, visible, and UV-visible illuminations. The previous study has shown that TiO_2 nanorods annealed at 500^{o}C exhibit

better photocatalytic activity than the as-deposited and annealed at 400°C TiO_2 nanorods.[41] In this work, we only study the photocatalytic activity of samples annealed at 500°C. The absorption spectra of MB solution were monitored over 4 hours and the change in the intensity of the MB absorption peak at λ = 664 nm is used to determine the decay rates by fitting the data to a pseudo-first-order decay equation,

$$\ln\frac{\alpha(0)}{\alpha(t)} = kt, \tag{6}$$

where $\alpha(0)$ and $\alpha(t)$ are the absorbance of MB at time t = 0 and t, and k is the decay rate. Fig. 7 shows the plots of $\ln[\alpha(0)/\alpha(t)]$ versus t for different X %Ag-TiO_2 composite nanorods annealed at 500°C and the solid lines are the fitting results under visible illumination. As described above, the increase in X % results in less TiO_2, shorter nanorods, and less surface area. In order to remove the effect of the surface area and only account for the effect of the Ag loading, the specific decay rate k', which is the decay rates k normalized by the average lengths of nanorods, is obtained. Here we assume that the decay rates are linearly proportional to the average nanorod length l,[47] which can be obtained by $l = h/\cos\beta$. The obtained specific decay rates are summarized in Table 2 and plotted in Fig. 8. As shown in Fig. 8, it is clear that $k'_{UV\text{-}Vis} > k'_{UV} + k'_{Vis}$ for all the Ag-TiO_2 samples. Under the same illumination, with increasing X %, the specific decay rate k' increases, reaches the maximum, and then decreases. k' reaches the maximum at X % = 15% under UV and UV-Vis illuminations and at X % = 10% under visible illumination.

Under visible illumination, though TiO_2 cannot be activated due to its large band gap, the

decay rate is not zero, and is mainly due to the self-photosensitization of MB.[48] The MB molecules can be activated by visible light. Then the excited electrons may be subsequently transferred into the conduction band of TiO_2 and react with the preadsorbed oxygen on the surface of TiO_2 , producing oxidizing species which may participate in the reaction of MB photodegradation as illustrated in Fig. 9 (a).[49] Compared to the pure TiO_2, the Ag-TiO_2 samples exhibit better photocatalytic performance under visible illumination. There are three possible mechanisms for such an observation. First, Ag NPs can absorb visible light due to LSPR and then inject the excited electrons into the conduction band of TiO_2 as illustrated in Fig. 9 (a). When the concentration of Ag is low, the increase of Ag loading results in larger interface area between TiO_2 and Ag, which facilitates the electron transfer and enhance the photocatalytic activity. However, as more Ag is loaded on TiO_2, less TiO_2 is exposed to MB molecules, which results in less electrons transferred from MB to TiO_2 and thus reduces the photocatalytic activity.

Another possible mechanism is that: the energy is transferred from photo-excited Ag NPs to TiO_2 in a radiative way through the interaction of TiO_2 with localized enhanced electric field, resulting in an increase of the electron-hole pair density.[19] However, if the energy of LSPR is lower than the band gap of TiO_2, no significant enhancement in photocatalytic activity can be observed.[50] As shown in the extinction spectra, the LSPR wavelength of Ag NPs is located between 500 nm and 700 nm, which is insufficient to activate TiO_2. Therefore, this radiative energy transfer may not lead to the enhanced photocatalytic activity.

Finally, Ag NPs can generate heat under optical illumination due to nonradiative decay of

surface plasmons into phonon modes. The localized heating and the temperature increase may contribute to the enhanced photocatalytic activity. The temperature increase ΔT_{tot} due to plasmon resonance can be estimated by a theory developed by Govorov et al., and is summarized in Table 2.[51] The calculation details can be found in Supporting Information (Part III). ΔT_{tot} increases with Ag concentration and reaches 3.2 K for 20%Ag-TiO_2. If the localized heating is the dominant mechanism in photodegradation of MB, 20%Ag-TiO_2 should have the highest decay rate, which do not occur in our experiment. So we assume that, the localized heating by Ag NPs is negligible and does not contribute significantly to the enhanced photocatalytic activity.

Upon UV illumination, TiO_2 is activated and generates electron-hole pairs. When Ag is loaded in TiO_2 matrix, the electrons in the conduction band of TiO_2 may be trapped by Ag NPs,[52] which is energetically favorable and suppresses the electron-hole recombination as illustrated in Fig. 9 (b). In addition, the accumulation of the trapped electrons in Ag NPs shifts the Fermi level more negative and makes Ag more reductive. The photogenerated electrons in TiO_2 and the trapped electrons in Ag react with the preadsorbed oxygen. The holes in the valence band of TiO_2 react with H_2O or OH^-. Both reactions finally generate hydroxyl radicals as illustrated in Fig. 9 (b),[49] which then degrade MB. Compared to the degradation under visible illumination in which electrons from MB and Ag play an important role, the degradation of MB under UV illumination is much faster because the TiO_2 matrix can generate more electron-hole pairs and both electrons and holes contribute to the degradation. More Ag loaded in TiO_2 increases the interface area and results in better charge separation and thus

better photocatalytic activity. The highest photocatalytic activity was observed with 15%Ag-TiO_2 under UV illumination. However, a higher concentration of Ag leads to decreased photocatalytic activity. As shown in the SEM images, 20%Ag-TiO_2 has more large Ag NPs than 15%Ag-TiO_2, limiting the exposure area of TiO_2 to UV illumination and MB molecules. Moreover, as more photogenerated electrons are accumulated in Ag, the probability of holes captured by these negatively charged nanoparticles increases significantly and decreases the efficiency of electron-hole separation, subsequently reducing the photocatalytic activity.

Under both UV and visible light illumination, faster degradation occurs for each sample compared with that under UV light. The visible light can excite both MB molecules and Ag NPs, resulting in self-photosensitization and hot electrons transferred to conduction band of TiO_2, respectively. In order to see the effect of the addition of visible light, the enhancement factor *EF*, defined as $EF = k'_{UV\text{-}Vis}/k'_{UV}$ is calculated for each sample and presented in Table 2. The *EF* is inversely related to the specific decay rate under visible illumination, which means a better photocatalytic performance under visible illumination will lead to a smaller enhancement under UV-Visible illumination. For the intrinsic TiO_2 sample, the maximum enhancement is achieved and is only due to the self-sensitization of MB. For the Ag-TiO_2 composite samples, the electron transfer has different direction under UV or visible illumination. When Ag-TiO_2 composite samples are under illumination of both UV and visible light, the photogenerated electrons in conduction band of TiO_2 can be trapped at Ag NPs and thus improve the life time of the holes in valence band of TiO_2. In the meantime, Ag can also be

excited by visible light and transfer electrons back to TiO_2, which prevents the charge separation in TiO_2 and leads to a negative impact on the photocatalytic activity.

4. Conclusion

Ag-TiO_2 composite nanorod arrays with different Ag concentrations have been fabricated by oblique angle co-deposition. TiO_2 is amorphous in the as-deposited samples and changes into anatase after annealing. As indicated by SEM and TEM images, Ag NPs are formed on and inside the TiO_2 matrix. By varying the concentration of Ag and the annealing condition, the size and the density of Ag NPs on the surface of TiO_2 can be tuned, and subsequently their optical properties. The addition of Ag in TiO_2 results in enhanced photocatalytic activity compared to pure TiO_2. Ag NPs play different roles in enhancing photocatalytic activity under different light sources. Under visible illumination, the Ag NPs are excited due to LSPR, and the electron transfer from Ag to TiO_2 is the primary contribution to the enhancement in photocatalytic activity. Under UV illumination, TiO_2 is activated and electron-hole pairs are generated, and Ag NPs work as electron traps, facilitating the charge separation and thus enhancing the photocatalytic activity. However, extra Ag loading beyond the optimal concentration leads to reduced photocatalytic activity mainly due to limited TiO_2 surface area exposed to dye molecules and the increased possibility of capture of holes by Ag NPs. Since the electron transfers are in the opposite direction under UV and visible illumination, the direct contact of Ag with TiO_2 may not result in a great enhancement in the photocatalytic performance. In order to improve the photocatalytic activity under UV-Vis illumination,

indirect contact of TiO_2 with Ag may be necessary to get rid of the back transfer of electrons to Ag.

Acknowledgements

We gratefully acknowledge the support from Savannah River National Laboratory LDRD-DOE program and partial support from the National Science Foundation (Grant No. ECCS-1029609).

Reference

1. A. Fujishima and K. Honda, *Nature*, 1972, **238**, 37-38.
2. P. Szymanski and M. A. El-Sayed, *Theor. Chem. Acc.*, 2012, **131**, 1202.
3. M. Ni, M. K. H. Leung, D. Y. C. Leung and K. Sumathy, *Renew. Sust. Energ. Rev.*, 2007, **11**, 401-425.
4. T. Inoue, A. Fujishima, S. Konishi and K. Honda, *Nature*, 1979, **277**, 637-638.
5. V. P. Indrakanti, J. D. Kubicki and H. H. Schobert, *Energy Environ. Sci.*, 2009, **2**, 745.
6. K. Koci, L. Obalova and Z. Lacny, *Chem. Pap.*, 2008, **62**, 1-9.
7. S. C. Roy, O. K. Varghese, M. Paulose and C. A. Grimes, *ACS Nano*, 2010, **4**, 1259-1278.
8. S. Sato, *Chem. Phys. Lett.*, 1986, **123**, 126-128.
9. S. Sato, R. Nakamura and S. Abe, *Appl. Catal. A-Gen.*, 2005, **284**, 131-137.
10. E. Borgarello, J. Kiwi, M. Gratzel, E. Pelizzetti and M. Visca, *J. Am. Chem. Soc.*, 1982, **104**, 2996-3002.
11. S. Klosek and D. Raftery, *J. Phys. Chem. B*, 2001, **105**, 2815-2819.
12. D. Behar and J. Rabani, *J. Phys. Chem. B*, 2006, **110**, 8750-8755.
13. B. Oregan and M. Gratzel, *Nature*, 1991, **353**, 737-740.
14. G. Marci, V. Augugliaro, M. J. Lopez-Munoz, C. Martin, L. Palmisano, V. Rives, M. Schiavello, R. J. D. Tilley and A. M. Venezia, *J. Phys. Chem. B*, 2001, **105**, 1026-1032.
15. A. Yamakata, T. Ishibashi and H. Onishi, *J. Phys. Chem. B*, 2002, **106**, 9122-9125.
16. L. W. Zhang, H. H. Mohamed, R. Dillert and D. Bahnemann, *J. Photochem. Photobiol. C-Photochem. Rev.*, 2012, **13**, 263-276.
17. M. A. Henderson, *Surf. Sci. Rep.*, 2011, **66**, 185-297.
18. Y. Tian and T. Tatsuma, *J. Am. Chem. Soc.*, 2005, **127**, 7632-7637.
19. K. Awazu, M. Fujimaki, C. Rockstuhl, J. Tominaga, H. Murakami, Y. Ohki, N. Yoshida and T. Watanabe, *J. Am. Chem. Soc.*, 2008, **130**, 1676-1680.
20. X. Chen, Z. F. Zheng, X. B. Ke, E. Jaatinen, T. F. Xie, D. J. Wang, C. Guo, J. C. Zhao and H. Y. Zhu, *Green Chem.*, 2010, **12**, 414-419.
21. L. Armelao, D. Barreca, G. Bottaro, A. Gasparotto, C. Maccato, E. Tondello, O. I. Lebedev, S. Turner, G. Van Tendeloo, C. Sada and U. L. Stangar, *ChemPhysChem*, 2009, **10**, 3249-3259.
22. D. Gong, W. C. J. Ho, Y. Tang, Q. Tay, Y. Lai, J. G. Highfield and Z. Chen, *J. Solid*

State Chem., 2012, **189**, 117-122.

23. W. Smith, S. Mao, G. H. Lu, A. Catlett, J. H. Chen and Y. P. Zhao, *Chem. Phys. Lett.*, 2010, **485**, 171-175.
24. A. Kedziora, W. Strek, L. Kepinski, G. Bugla-Ploskonska and W. Doroszkiewicz, *J. Sol-Gel Sci. Technol.*, 2012, **62**, 79-86.
25. M. S. Lee, S.-S. Hong and M. Mohseni, *J. Mol. Catal. A: Chem.*, 2005, **242**, 135-140.
26. Y. P. He, Y. P. Zhao and J. S. Wu, *Appl. Phys. Lett.*, 2008, **92**, 063107.
27. Y. P. He, Z. Y. Zhang, C. Hoffmann and Y. P. Zhao, *Adv. Funct. Mater.*, 2008, **18**, 1676-1684.
28. G. K. Larsen, R. Fitzmorris, J. Z. Zhang and Y. P. Zhao, *J. Phys. Chem. C*, 2011, **115**, 16892-16903.
29. G. K. Larsen, B. C. Fitzmorris, C. Longo, J. Z. Zhang and Y. P. Zhao, *J. Mater. Chem.*, 2012, **22**, 14205-14218.
30. Y. P. He, C. Brown, Y. Z. He, J. G. Fan, C. A. Lundgren and Y. P. Zhao, *Chem. Commun.*, 2012, **48**, 7741-7743.
31. Y. P. He, C. Brown, C. A. Lundgren and Y. P. Zhao, *Nanotechnology*, 2012, **23**, 365703.
32. Y. He, J. G. Fan and Y. P. Zhao, *Cryst. Growth Des.*, 2010, **10**, 4954-4958.
33. Y. P. He and Y. P. Zhao, *Nanoscale*, 2011, **3**, 2361-2375.
34. A. C. van Popta, J. Cheng, J. C. Sit and M. J. Brett, *J. Appl. Phys.*, 2007, **102**, 013517.
35. J. D. Driskell, S. Shanmukh, Y. Liu, S. B. Chaney, X. J. Tang, Y. P. Zhao and R. A. Dluhy, *J. Phys. Chem. C*, 2008, **112**, 895-901.
36. Y. Zhao, Y. He and C. Brown, *Appl. Phys. Lett.*, 2012, **100**, 033106.
37. M. Jose-Yacaman, C. Gutierrez-Wing, M. Miki, D. Q. Yang, K. N. Piyakis and E. Sacher, *J. Phys. Chem. B*, 2005, **109**, 9703-9711.
38. W. Cai, H. Zhong and L. Zhang, *J. Appl. Phys.*, 1998, **83**, 1705.
39. W. E. Garner and L. W. Reeves, *Trans. Faraday Soc.*, 1954, **50**, 254-260.
40. H. E. Chao, Y. U. Yun, H. U. Xingfang and A. Larbot, *J. Eur. Ceram. Soc.*, 2003, **23**, 1457-1464.
41. Y. P. He, Z. Y. Zhang and Y. P. Zhao, *J. Vac. Sci. Technol., B: Microelectron. Nanometer Struct.--Process., Meas., Phenom.*, 2008, **26**, 1350.
42. X. Li, L. Wang and X. Lu, *J. Hazard. Mater.*, 2010, **177**, 639-647.
43. J.-Y. Park, K.-J. Hwang, J.-W. Lee and I.-H. Lee, *J. Mater. Sci.*, 2011, **46**, 7240-7246.

44. T. Choy, *Effective Medium Theory: Principles and Applications*, Oxford Univ Press, 1999.

45. G. B. Smith, *Opt. Commun.*, 1989, **71**, 279-284.

46. G. B. Smith, *Appl. Opt.*, 1990, **29**, 3685.

47. W. Smith, W. Ingram and Y. Zhao, *Chem. Phys. Lett.*, 2009, **479**, 270-273.

48. D. Chatterjee, S. Dasgupta and N. N. Rao, *Sol. Energy Mater. Sol. Cells*, 2006, **90**, 1013-1020.

49. T. X. Wu, G. M. Liu, J. C. Zhao, H. Hidaka and N. Serpone, *J. Phys. Chem. B*, 1998, **102**, 5845-5851.

50. D. B. Ingram and S. Linic, *J. Am. Chem. Soc.*, 2011, **133**, 5202-5205.

51. A. O. Govorov, W. Zhang, T. Skeini, H. Richardson, J. Lee and N. A. Kotov, *Nanoscale Res. Lett.*, 2006, **1**, 84-90.

52. A. Takai and P. V. Kamat, *ACS Nano*, 2011, **5**, 7369-7376.

Figure legends

Fig. 1 The representative SEM images of TiO_2 and Ag NP embedded TiO_2 composite nanorod arrays and the size distributions of Ag NPs. The scale bar in each SEM image represents 1 μm.

Fig. 2 The nanorod tilting angle β and height h versus the measured Ag atomic ratio X' %.

Fig. 3 The representative TEM images of 20%Ag-TiO_2 nanorods: (a) as-deposited and (b) annealed at $T = 500^oC$. Each scale bar represents 100 nm.

Fig. 4 XRD spectra of TiO_2 and Ag NP embedded TiO_2 composite nanorod arrays: (a) as-deposited, (b) annealed at $T = 400^oC$, and (c) annealed at $T = 500^oC$. The symbol "A" and "S" represent the XRD peaks of anatase TiO_2 and crystalline Ag, respectively.

Fig. 5 Unpolarized optical extinction spectra of both TiO_2 and Ag-TiO_2 nanorod arrays: (a) as-deposited, (b) annealed at $T = 400^oC$, and (c) annealed at $T = 500^oC$.

Fig. 6 First row: absorption coefficient predicted by EMT. Second row: polarized extinction spectra of nanorod films annealed at $T = 500^oC$.

Fig. 7 Photocatalytic MB degradation kinetics under visible light illumination for the samples annealed at $T = 500^oC$.

Fig. 8 Specific photodegradation rate k' of the samples annealed at $T = 500^oC$ under different illumination versus the designed Ag atomic ratio X %.

Fig. 9 The schematics of photocatalytic mechanism: (a) under visible light, and (b) under UV

light.

Samples	r_{Ag} (Å/s)	r_{TiO_2} (Å/s)	Predicted *X* %	Measured *X'* %	Height *h* (μm)	Tilting angle β (^{o})
TiO_2	0	3.5	0%	-	1.48 ± 0.05	55 ± 2
5%Ag-TiO_2	0.1	3.5	5%	9.4 ± 0.5%	1.21 ± 0.04	57 ± 2
10%Ag-TiO_2	0.2	3.3	10%	15 ± 2%	1.18 ± 0.02	58 ± 1
15%Ag-TiO_2	0.3	3.1	15%	22 ± 1%	1.10 ± 0.03	59 ± 1
20%Ag-TiO_2	0.4	2.9	20%	25.7 ± 0.6%	1.08 ± 0.03	59 ± 1

Table 1 Composition and morphology parameters for the as-deposited samples.

Samples		TiO_2	5%Ag -TiO_2	10%Ag-TiO_2	15%Ag-TiO_2	20%Ag-TiO_2
As-deposited	D_{NP} (nm)	-	40 ± 20	60 ± 30	70 ± 30	70 ± 50
	n_{NP} (μm^{-2})	-	5.3	5.4	6.6	5.3
***T* = 400°C**	D_{NP} (nm)	-	30 ± 10	50 ± 20	50 ± 20	50 ± 30
	n_{NP} (μm^{-2})	-	19.8	23.9	24.5	30.0
	TiO_2 grain size (nm)	16.7	17.2	13.7	14.0	14.1
***T* = 500°C**	D_{NP} (nm)	-	40 ± 20	40 ± 30	50 ± 50	70 ± 70
	n_{NP} (μm^{-2})	-	8.5	10.6	11.6	11.4
	TiO_2 grain size (nm)	16.7	18.6	14.2	15.5	14.1
	k'_{Vis} ($h^{-1}\mu m^{-1}$)	0.013	0.021	0.028	0.020	0.018
	k'_{UV} ($h^{-1}\ \mu m^{-1}$)	0.083	0.088	0.1006	0.114	0.086
	$k'_{UV\text{-}Vis}$ ($h^{-1}\ \mu m^{-1}$)	0.150	0.157	0.170	0.179	0.154
	Local temperature increase ΔT_{tot} (K)	-	0.45	0.57	1.2	3.2
	$EF = k'_{UV\text{-}Vis} / k'_{UV}$	1.81	1.79	1.69	1.57	1.78

Table 2 Sizes and densities of Ag nanoparticles on surfaces of nanorods, average grain sizes for TiO_2 anatase phase for the annealed samples and the specific photodegradation rates, the temperature increase on the surface of nanorods calculated by Eq. S14, and the photocatalytic reaction enhancement factors for the samples annealed at $T = 500^oC$.

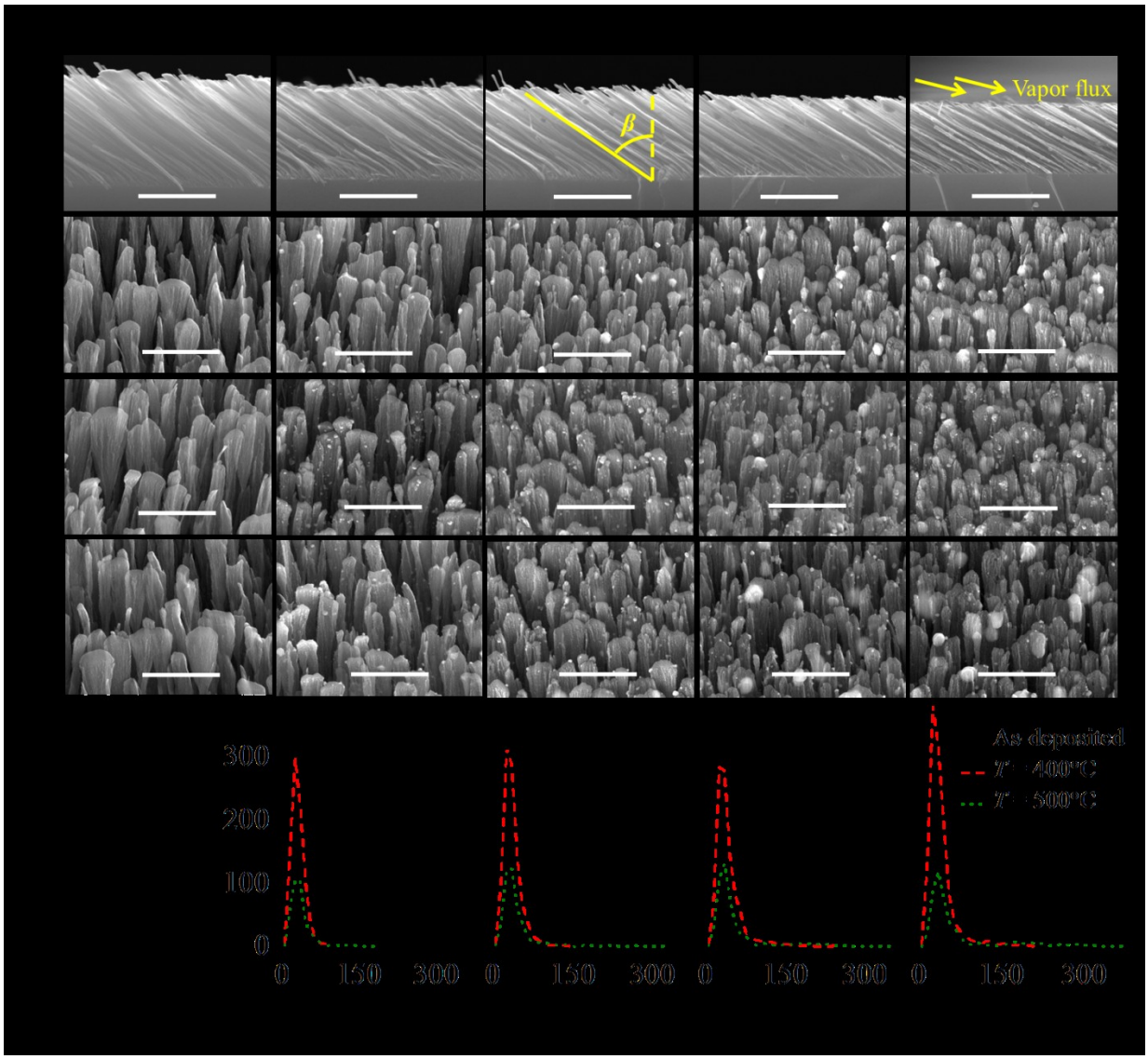

Fig. 1 He et al.

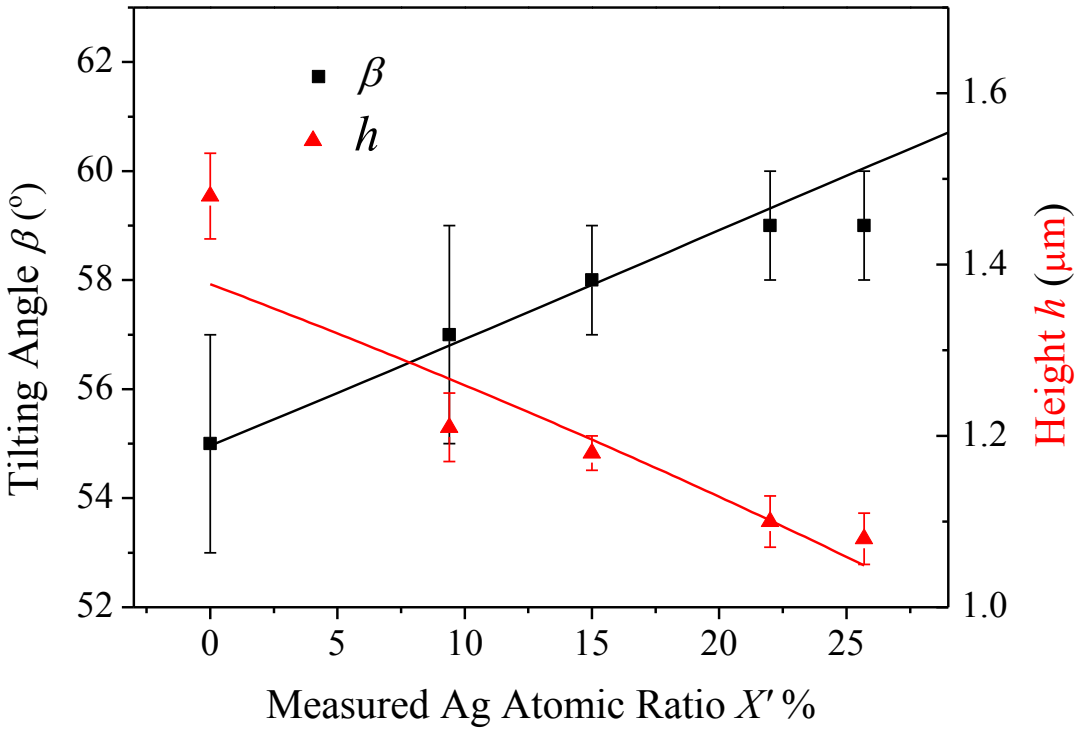
β
h
62
60
58
56
54
52
1.6
1.4
1.2
1.0
0
5
10
15
20
25
Tilting Angle β (°)
Height h (μm)
Measured Ag Atomic Ratio X′ %

Fig. 2 He et al.

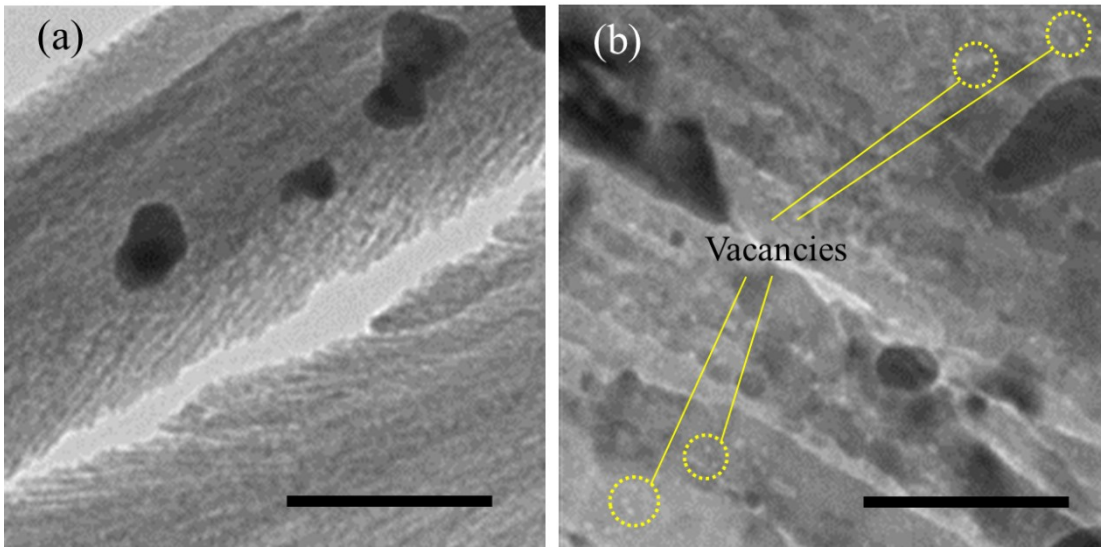

Fig. 3 He et al.

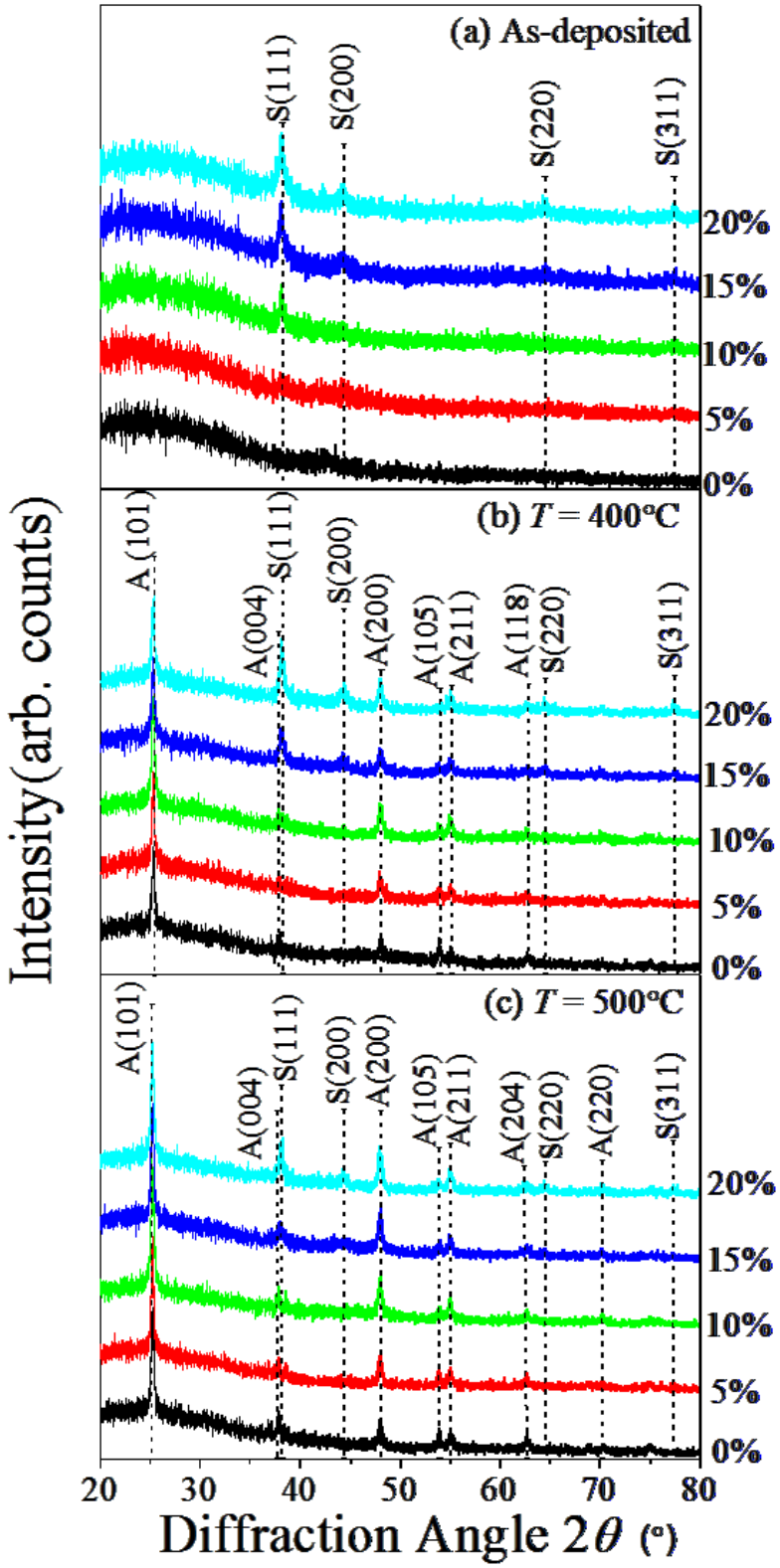
(a) As-deposited
S(111)
S(200)
S(220)
S(311)
20%
15%
10%
5%
0%
(b) T = 400°C
A(101)
A(004)
S(111)
S(200)
A(200)
A(105)
A(211)
A(118)
S(220)
S(311)
20%
15%
10%
5%
0%
(c) T = 500°C
A(101)
A(004)
S(111)
S(200)
A(200)
A(105)
A(211)
A(204)
S(220)
A(220)
S(311)
20%
15%
10%
5%
0%
Intensity(arb. counts)
20
30
40
50
60
70
80
Diffraction Angle 2θ (°)

Fig. 4 He et al.

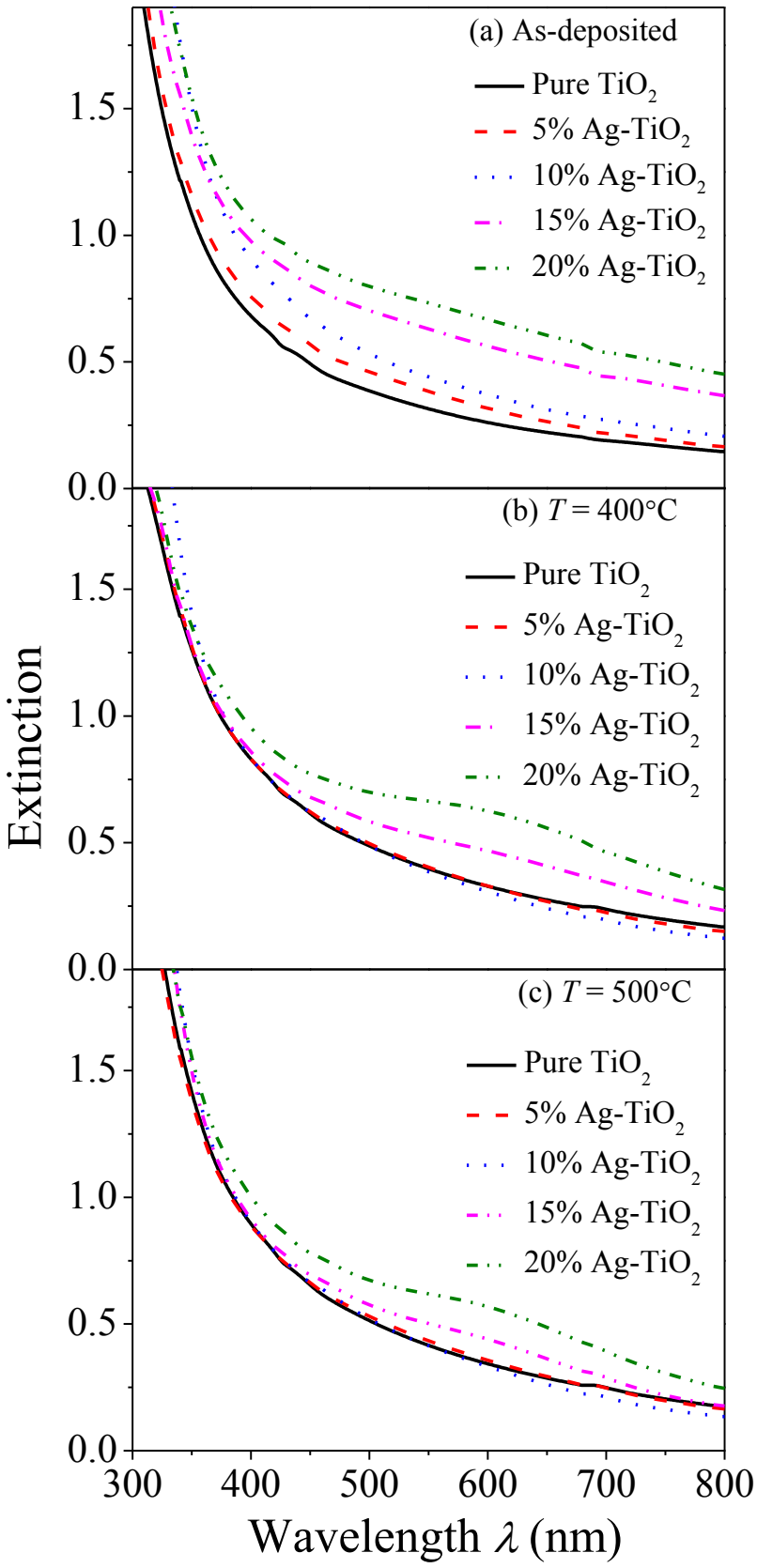
(a) As-deposited
Pure TiO2
5% Ag-TiO2
10% Ag-TiO2
15% Ag-TiO2
20% Ag-TiO2
(b) T = 400°C
(c) T = 500°C
Extinction
Wavelength λ (nm)
0.0
0.5
1.0
1.5
300
400
500
600
700
800

Fig. 5 He et al.

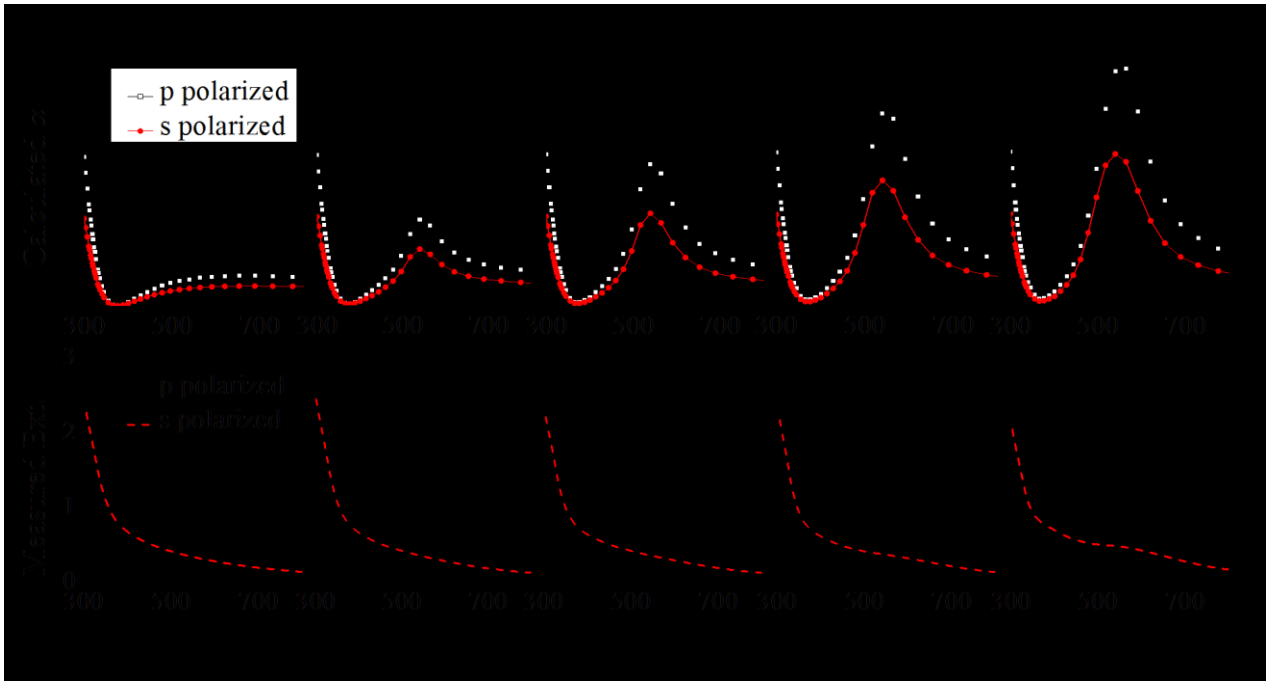

Fig. 6 He et al.

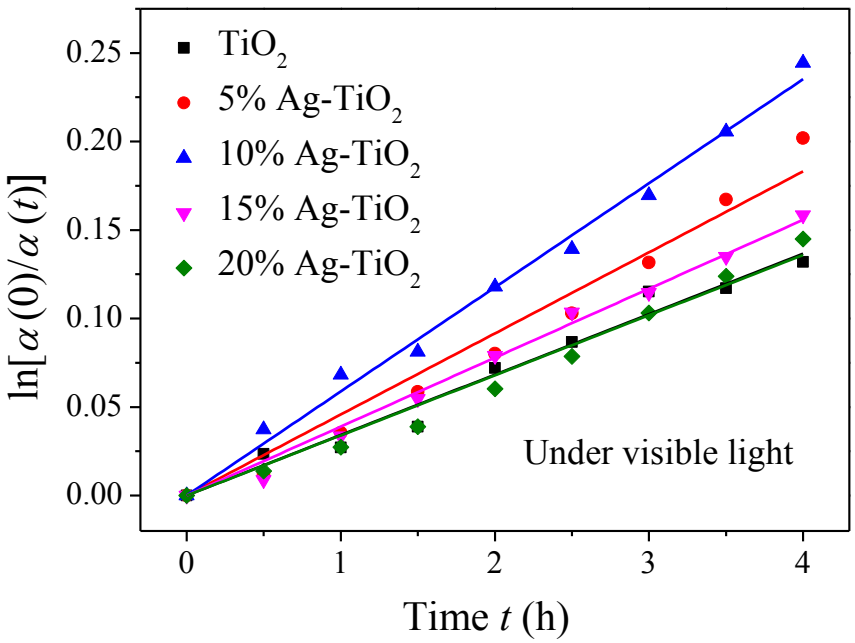
TiO2
5% Ag-TiO2
10% Ag-TiO2
15% Ag-TiO2
20% Ag-TiO2
Under visible light
ln[α(0)/α(t)]
Time t (h)
0.25
0.20
0.15
0.10
0.05
0.00
0
1
2
3
4

Fig 7. He et al.

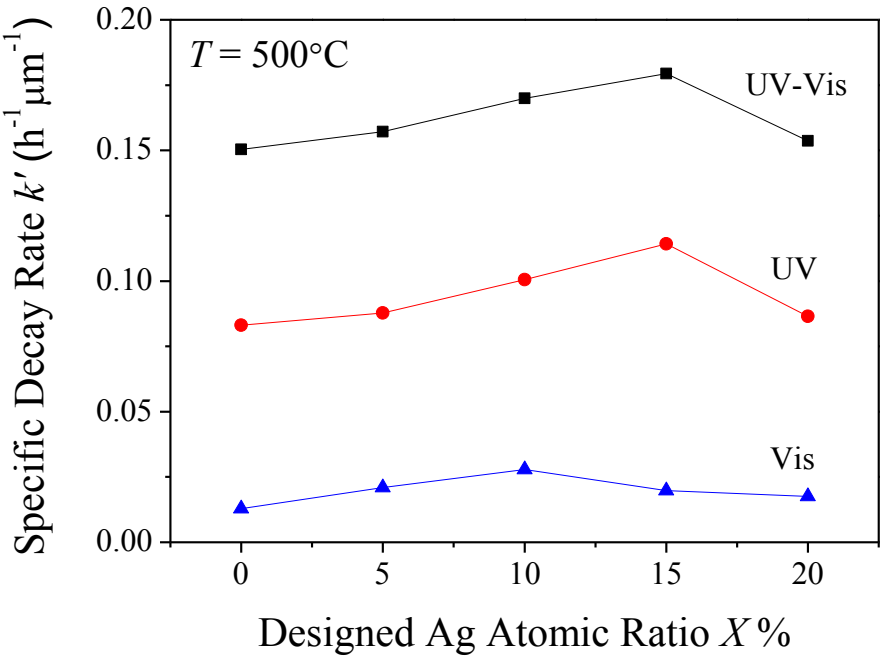
T = 500°C
UV-Vis
UV
Vis
Specific Decay Rate k′ (h-1μm-1)
Designed Ag Atomic Ratio X %
0.00
0.05
0.10
0.15
0.20
0
5
10
15
20

Fig 8. He et al.

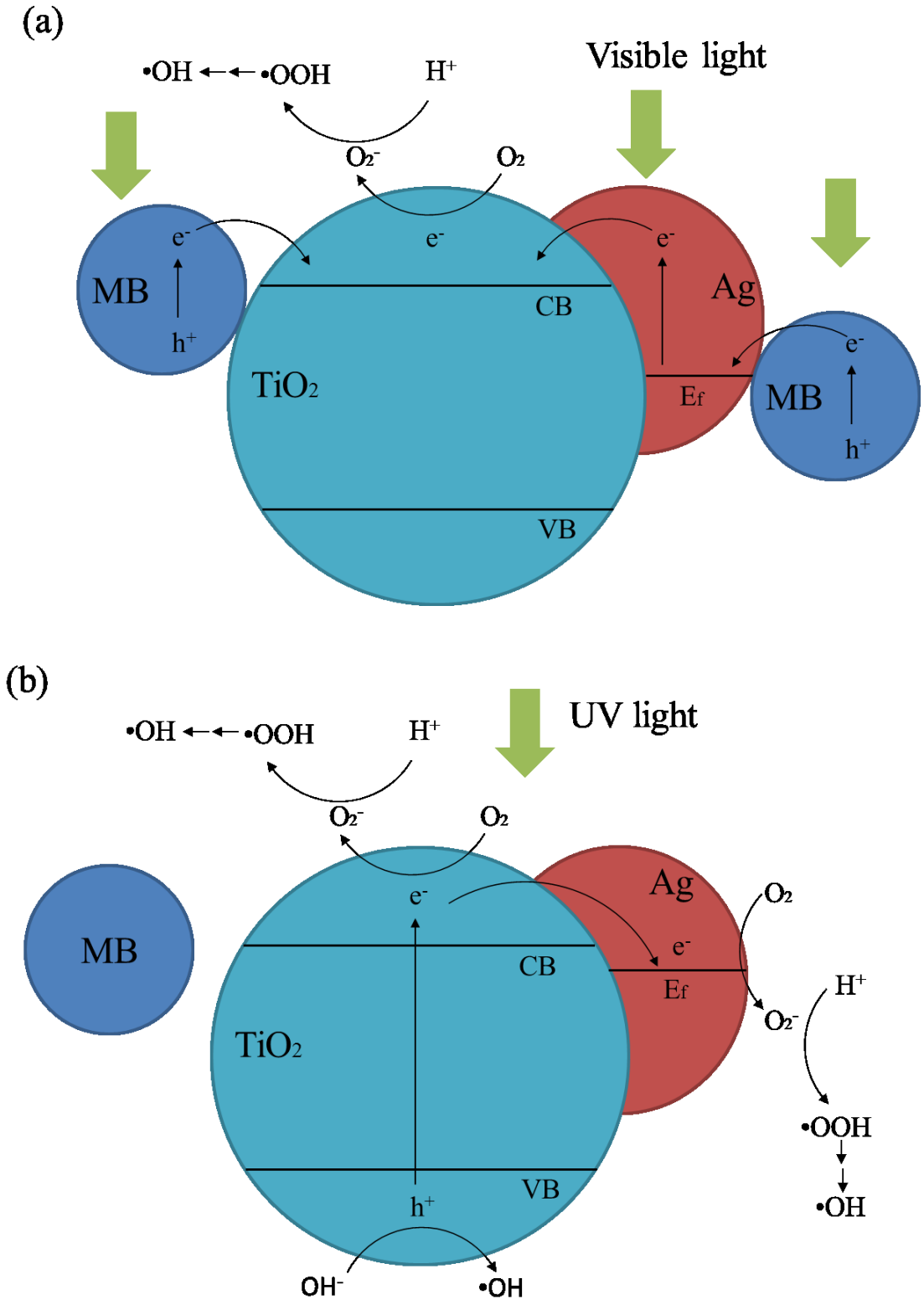
(a)
•OH ← ← •OOH
H+
Visible light
O2-
O2
e-
e-
e-
MB
h+
CB
Ag
TiO2
Ef
MB
e-
h+
VB
(b)
•OH ← ← •OOH
H+
UV light
O2-
O2
Ag
e-
O2
MB
CB
e-
Ef
TiO2
H+
O2-
•OOH
•OH
VB
h+
OH-
•OH

Fig. 9 He et al.

Supporting Information

I. EDX spectra of Ag-TiO_2 composite nanorod arrays

The EDX spectra of Ag-TiO_2 composite nanorod arrays are shown in Figure S1. In the spectra, the strongest peak is from Si support substrates. The EDX peaks corresponding to O, Ag, and Ti are all observed. As the designed atomic ratio of Ag increases, the intensity of Ag peak increases while the intensity of Ti peak almost remains the same, indicating an increased concentration of Ag in the composite thin films.

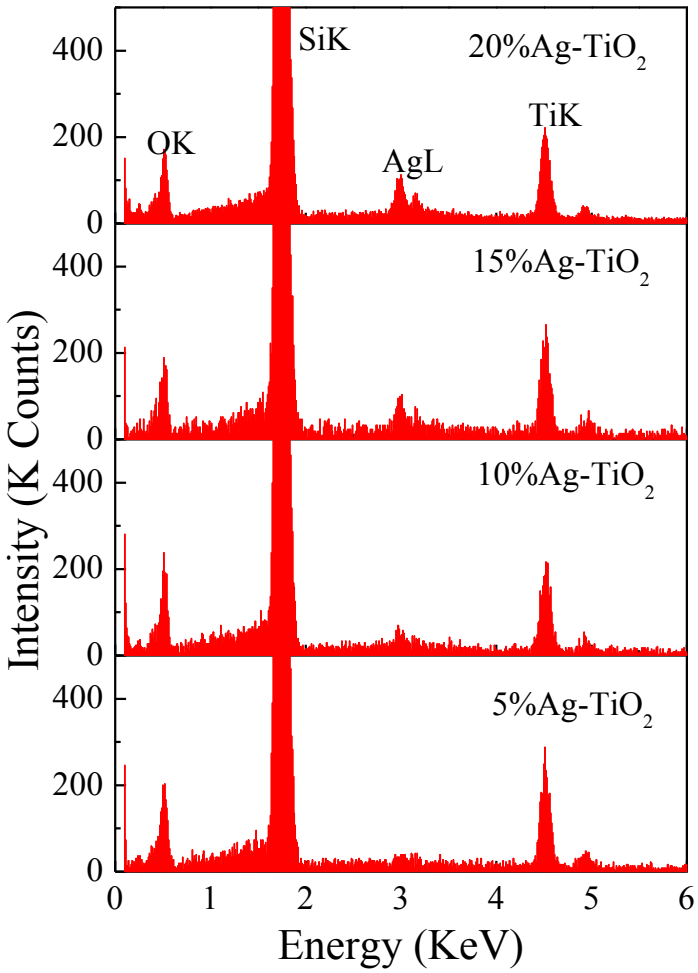

Fig. S1 EDX spectra of as-deposited Ag NP embedded TiO_2 composite samples

II. Estimation of optical properties of Ag-TiO_2 nanorod arrays by effective medium theory

To estimate the optical properties of Ag NP embedded TiO_2 by effective medium theory (EMT), the nanorods can be treated as prolate spheroids with diameter D, length L, and tilting angle β with respect to the normal of the substrate. The linearly s- or p-polarized light is incident normal to the

substrate as illustrated in Fig. S2 and the nanorods are in the y-z plane. The dielectric tensor ε in the global coordinate (x, y, z) can be related to the tensor ε' in the local coordinate (x', y', z'),

$$\varepsilon' = \begin{pmatrix} \varepsilon_{x'} & 0 & 0 \\ 0 & \varepsilon_{y'} & 0 \\ 0 & 0 & \varepsilon_{z'} \end{pmatrix} = \begin{pmatrix} \varepsilon_O & 0 & 0 \\ 0 & \varepsilon_O & 0 \\ 0 & 0 & \varepsilon_E \end{pmatrix}. \quad \text{(S1)}$$

The dielectric constants for both s- and p-polarized incident light can be expressed as,

$$\varepsilon_s = \varepsilon_O, \quad \text{(S2)}$$

$$\varepsilon_p = \frac{\varepsilon_E \varepsilon_O}{\varepsilon_O \sin^2 \beta + \varepsilon_E \cos^2 \beta}. \quad \text{(S3)}$$

In order to obtain ε_O and ε_E, the EMT is used twice, first to calculate the dielectric constants of Ag NP embedded TiO_2 bulk material, and then to use calculated dielectric constants to obtain the effective dielectric constants of nanorods with voids.

Maxwell-Garnett (MG) approximation is used to calculate the effective refractive index of Ag NP embedded TiO_2 bulk material,

$$\frac{\varepsilon_{Ag-TiO_2} - \varepsilon_{TiO_2}}{\varepsilon_{TiO_2} + L_1(\varepsilon_{Ag-TiO_2} - \varepsilon_{TiO_2})} = f_{Ag}\left[\frac{\varepsilon_{Ag} - \varepsilon_{TiO_2}}{\varepsilon_{TiO_2} + L_1(\varepsilon_{Ag} - \varepsilon_{TiO_2})}\right], \quad \text{(S4)}$$

where ε_{TiO_2} and ε_{Ag} are the dielectric constants of TiO_2 and Ag respectively, f_{Ag} is the volume fraction of Ag and L_1 is depolarization factor. $L_1 = 1/3$ for spherical particles of Ag.

Then Bruggeman (Br) approximation was applied to calculate the effective refractive index of the Ag-TiO_2 composite nanorod arrays, which are composed of nanorods and void,

$$f_{rod}\left[\frac{\varepsilon_{Ag-TiO_2} - \varepsilon_{array}}{\varepsilon_{array} + L_2^i(\varepsilon_{Ag-TiO_2} - \varepsilon_{array})}\right] + (1 - f_{rod})\left[\frac{\varepsilon_{void} - \varepsilon_{array}}{\varepsilon_{array} + L_2^i(\varepsilon_{void} - \varepsilon_{array})}\right] = 0, \quad \text{(S5)}$$

for $i = x', y', z'$, where f_{rod} is the volume fraction of nanorods. The volume fractions

are listed in Table S1. The depolarization factor can be calculated as,[1]

$$L_2^{z'} = \frac{1-e^2}{e^2}\left[\frac{1}{2e}\ln\left(\frac{1+e}{1-e}\right)-1\right], \quad \text{(S6)}$$

$$e = \sqrt{1-\left(\frac{D}{L}\right)^2}, \quad \text{(S7)}$$

$$L_2^{x'} = L_2^{y'} = \frac{1}{2}(1-L_2^{z'}). \quad \text{(S8)}$$

By combining Eqs. S4-S8, ε_O and ε_E can be obtained and then ε_s and ε_p are calculated according to Eqs. S2 & S3. The complex refractive index of the composite nanorod structures can be extracted, and thus the absorption coefficient α can be obtained by,

$$\alpha(\omega) = \frac{2\omega}{c}\kappa(\omega) \quad \text{(S9)}$$

where $\kappa(\omega)$ is the imaginary index of refraction obtained from above calculations.

***X* %**	**5%**	**10 %**	**15 %**	**20 %**
f_{Ag}	0.02 8	0.05 7	0.08 8	0.12 1
f_{rod}	0.5	0.5	0.5	0.5

Table S1 Ag volume fractions f_{Ag} and nanorod volume fractions f_{rod} in EMT calculation

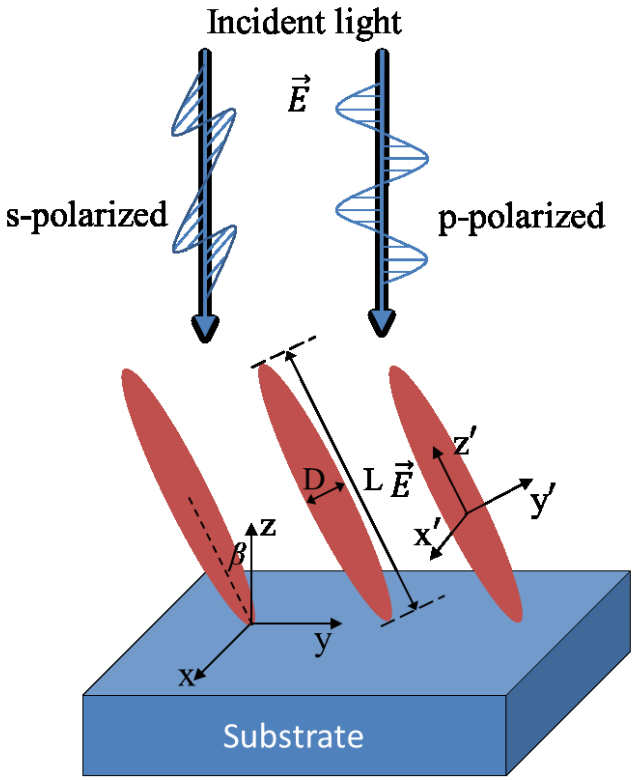

Fig. S2 Schematic of Ag NP embedded TiO_2 nanorod arrays under the s- or p-polarized incident light.

III. Estimation of the temperature increase of Ag NPs on TiO_2 nanorod under visible light

Following the theory by Govorov et al., the temperature increase ΔT_{NP} on the surface of a single Ag particle caused by plasmon resonance can be expressed as, [2, 3]

$$\Delta T_{NP}(I_0) = \frac{R_{NP}^2}{3k_0}\frac{\omega}{8\pi}\left|\frac{3\varepsilon_0}{2\varepsilon_0+\varepsilon_{NP}}\right|^2 \mathrm{Im}\,\varepsilon_{NP}\frac{8\pi I_0}{c\sqrt{\varepsilon_0}}, \quad \text{(S10)}$$

where I_0 is the light intensity, ω is the angular frequency of the incident light, k_0 and ε_0 are the thermal conductivity and the dielectric function of the surrounding, R_{NP} and ε_{NP} are the radius and the dielectric function of nanoparticles, respectively. For Ag-TiO_2 composite nanorods in MB solution, only the Ag NPs on the surface of TiO_2 need to be considered. For simplicity, we assume,

$$\varepsilon_0 = \frac{\varepsilon_{H_2O}+\varepsilon_{TiO_2}}{2}, \quad \text{(S11)}$$

$$\varepsilon_{NP} = \varepsilon_{Ag}, \quad \text{(S12)}$$

$$k_0 = \frac{k_{H_2O}+k_{TiO_2}}{2}, \quad \text{(S13)}$$

where ε_{H_2O}, ε_{TiO_2}, and ε_{Ag} are the dielectric functions of bulk H_2O, TiO_2, and Ag, respectively, and k_{H_2O} and k_{TiO_2} are the thermal conductivity of H_2O and TiO_2. With incident light at wavelength λ with intensity of 65 mW/cm^2, the temperature increase ΔT_{NP} at the surface of a single nanoparticle is calculated, and plotted as function of λ as shown in Fig. S3. ΔT_{NP} exhibits a significant dependence on λ and reaches a maximum at λ_{max} = 477 nm, which originates from the plasmon resonance of Ag NPs. In our photodegradation experiment, the visible illumination is a broad-band light (400 nm ~ 800

nm) with total intensity of 65 mW/cm^2. In order to estimate the maximum ΔT_{NP} in the experiment, we assume that only the light in wavelength range of 425 nm ~ 525 nm contributes to the temperature increase, and ΔT_{NP} is a constant in this wavelength range and equal to the temperature increase at λ_{max}. The light intensity in this wavelength range is about 9.8 mW/cm^2 according to the spectrum of the visible light. With this light intensity, the actual temperature increases at the surface of a single Ag NP ΔT_{NP} can be estimated and are shown in Table S2.

The Ag-TiO_2 composite nanorod arrays consist of large numbers of nanoparticles. The total temperature increase within the nanostructure ΔT_{tot} can be expressed as follows:[2]

$$\Delta T_{tot} \approx \Delta T_{NP} \frac{R_{NP}}{\Delta r} N_{NP}^{2/3}, \qquad \text{(S14)}$$

where Δr is the average separation between nanoparticles and N_{NP} is the number of nanoparticles. The N_{NP} can be estimated by,

$$N_{NP} = n_{NP} A_{surface}, \qquad \text{(S12)}$$

where n_{NP} is the number density of Ag NPs and $A_{surface}$ is the total surface area of each sample. Assuming the particles are uniformly distributed in the nanorod arrays, the separation between particles Δr can be calculated by:

$$\frac{1}{\Delta r^3} = \frac{N_{NP}}{A_{sub} h}, \qquad \text{(S13)}$$

where A_{sub} is the substrate area and is about 2.0 cm^2. The maximum total temperature increases ΔT_{tot} can be calculated and are listed in Table S2.

***X* %**	**5%**	**10%**	**15%**	**20%**
R_{NP} (nm)	20	20	25	35
n_{NP} (μm^{-2})	8.5	10.6	11.6	11.4
N_{NP} ($x10^9$)	2.05	2.54	2.74	2.70
$A_{surface}$ (x 10^3 mm^2)	2.4	2.4	2.3	2.3
Δr (nm)	228	210	202	203
ΔT_{NP} ($x10^{-7}$ K)	6.9	6.9	10.8	21.2

Table S2 Parameters used to estimate the temperature increase

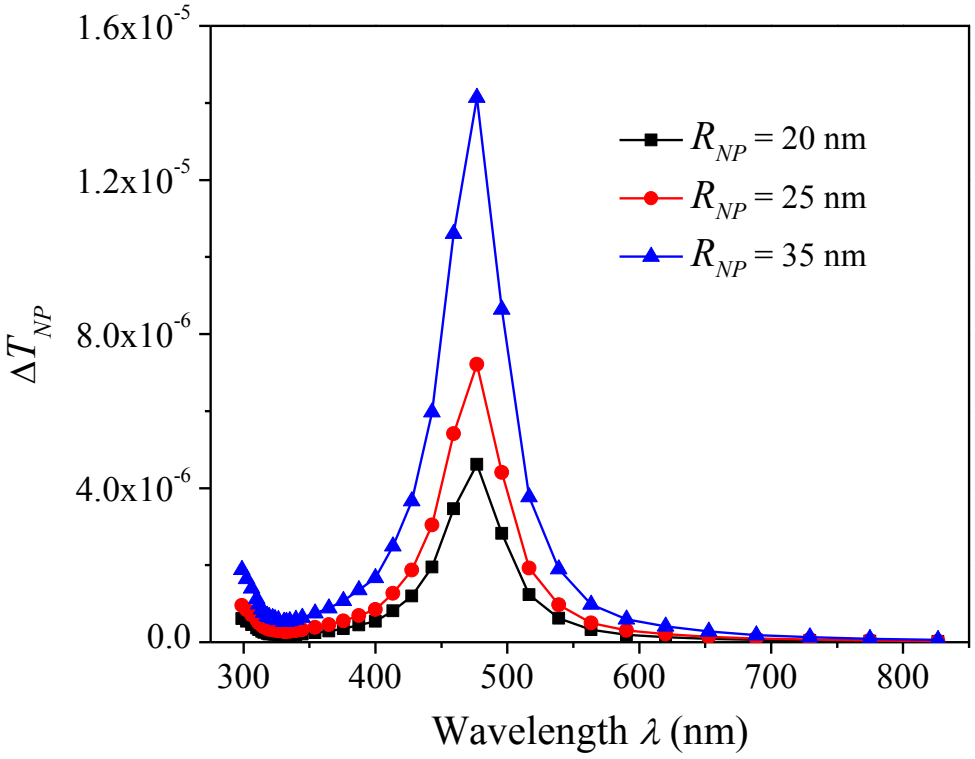

Fig. S3 The temperature increase at the surface of a single Ag nanoparticle ΔT_{NP} as functions of wavelength with different nanoparticle radii R_{NP}

Reference

1. C. Bohren and D. Huffman, *Absorption and Scattering of Light by Small Particles*, Wiley-VCH, 1998.
2. A. O. Govorov, W. Zhang, T. Skeini, H. Richardson, J. Lee and N. A. Kotov, *Nanoscale Res. Lett.*, 2006, **1**, 84-90.
3. A. O. Govorov and H. H. Richardson, *Nano Today*, 2007, **2**, 30-38.